magnetochemistry

MDPI

Article

Counterintuitive Single-Molecule Magnet Behaviour in Two Polymorphs of One-Dimensional Compounds Involving Chiral BINOL-Derived Bisphosphate Ligands

Carlo Andrea Mattei , Bertrand Lefeuvre, Vincent Dorcet, Gilles Argouarch, Olivier Cador, Claudia Lalli and Fabrice Pointillart *

ISCR (Institut des Sciences Chimiques de Rennes)—UMR 6226, CNRS, University of Rennes, 35042 Rennes, France; carloandrea22@libero.it (C.A.M.); bertrand.lefeuvre@univ-rennes1.fr (B.L.); vincent.dorcet@univ-rennes1.fr (V.D.); gilles.argouarch@univ-rennes1.fr (G.A.); olivier.cador@univ-rennes1.fr (O.C.); claudia.lalli@univ-rennes1.fr (C.L.)

* Correspondence: fabrice.pointillart@univ-rennes1.fr

Abstract: The coordination reaction of the [Dy(hfac)$_3$(H$_2$O)$_2$] units (hfac$^-$ = 1,1,1,5,5,5-hexafluoroacetylacetonate) with the [8′-(Diphenoxylphosphinyl)[1,1′-binaphthalen]-8-yl]diphenoxylphosphine oxide ligand (**L**) followed by a crystallisation in a 1:3 CH$_2$Cl$_2$:*n*-hexane solvent mixture led to the isolation of a new polymorph of formula [(Dy(hfac)$_3$((*S*)-L))$_3$]$_n$ (**1**). The X-ray structure on single crystal of **1** revealed the formation of a mono-dimensional coordination polymer with three crystallographically independent Dy^{III} centres, which crystallised in the polar chiral P2$_1$ space group. Ac magnetic measurements highlighted single-molecule magnet behaviour under both zero and 1000 Oe applied magnetic field with magnetic relaxation through quantum tunneling of the magnetisation (QTM, zero field only) and Raman processes. Despite the three crystallographically independent Dy^{III} centres adopting a distorted D$_{4d}$ coordination environment, a single slow magnetic relaxation contribution was observed at a slower rate than its previously studied [(Dy(hfac)$_3$((*S*)-L))]$_n$ (**2**) polymorph.

Keywords: dysprosium; β-diketonate; binaphtyl; polymorphs; chirality; single-molecule magnets

check for updates

Citation: Mattei, C.A.; Lefeuvre, B.; Dorcet, V.; Argouarch, G.; Cador, O.; Lalli, C.; Pointillart, F. Counterintuitive Single-Molecule Magnet Behaviour in Two Polymorphs of One-Dimensional Compounds Involving Chiral BINOL-Derived Bisphosphate Ligands. *Magnetochemistry* **2021**, *7*, 150. https://doi.org/10.3390/magnetochemistry7110150

Academic Editor: Salah Massoud

Received: 12 October 2021
Accepted: 11 November 2021
Published: 16 November 2021

1. Introduction

Single-molecule magnets (SMMs) have fascinated communities of chemists and physicists for the last 30 years because they display slow magnetic relaxation with magnetic bistability and quantum behaviours at low temperatures [1,2]. The latter opens the door to potential applications in molecular spintronics [3–7], quantum computing [8–12] and magneto-optics [13]. The discovery of lanthanide SMMs [14] with blocking temperatures for the reversal magnetisation up to 80 K [15], push back SMMs into the race of applications in high-density data storage [16,17].

To magnetism, another physical property can be added to achieve multi-property materials [18–25]. In this context, the addition of the chirality is probably the most popular choice because it leads to the observation of multiferroic materials [26–29], for instance when ferromagnetism cohabits with ferroelectricity and magneto-chiral anisotropy [30–33]. In the particular case of SMM behaviour, the addition of chirality could lead to the observation of circularly polarised luminescent SMMs [34–37], ferroelectric SMMs [38–42], magnetoelectric coupling in SMMs [43] and magneto-chiral SMMs [44,45]. A few years ago, some of us demonstrated that chirality can indirectly modulate the SMM behaviour through the change of dipolar interaction due to different crystal packings in the racemic SMM mixture and enantiopure SMM [46].

Polymorphism could also play a crucial role in the modulation of the SMM behaviour because it could induce changes in the intermolecular interaction (dipolar magnetic interaction), and local environment of the metal (crystal field) [47,48].

Recently, the (chir)optical and magnetic properties of $[Dy(hfac)_3((S)\text{-}L)]_n$ (**2**) (L = Diphenoxylphosphinyl)[1,1′-binaphthalen]-8-yl]diphenoxylphosphine oxide) (Scheme 1) were studied [49,50]. A new polymorph of formula $[(Dy(hfac)_3((S)\text{-}L))_3]_n$ (**1**) was then isolated, and its magnetic properties are presented here and compared to those of **2**.

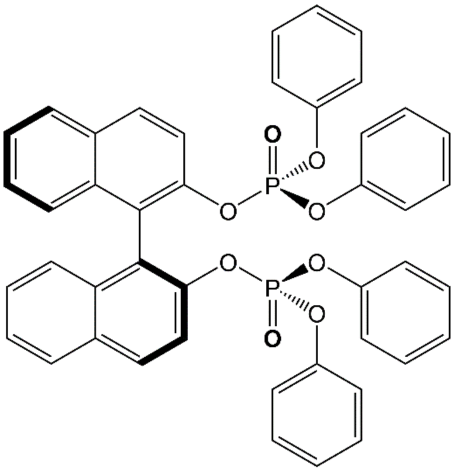

Scheme 1. Molecular structure of (*S*)-L.

2. Results and Discussion

2.1. Synthesis

The coordination reaction between the ligand (*S*)-L and the precursor $Dy(hfac)_3(H_2O)_2$ led to the formation of a mono-dimensional polymer of formula $[Dy(hfac)_3((S)\text{-}L)]_n$ (**2**) [49]. The polycrystalline powder of the latter polymer was obtained by slow diffusion of a large excess of *n*-hexane into a CH_2Cl_2 solution of **2** (CH_2Cl_2/*n*-hexane 1:40), while a slow evaporation from a solution of the reagents in CH_2Cl_2 quantitatively yielded the new polymorph of formula $[(Dy(hfac)_3((S)\text{-}L))_3]_n$ (**1**) as single crystal suitable for X-ray diffraction study and confirmed by PXRD studies.

2.2. X-ray Structures

XRD studies on single crystal revealed that the *S* form of this further product crystallises in the space group $P2_1$ (No. 4) with formula $[(Dy(hfac)_3((S)\text{-}L))_3]_n$ (**1**) (Table S1), while our previous work concluded that the mono-dimensional polymorph **2** crystallised in the chiral orthorhombic space group $C222_1$ (N°20)[49]. It is worthwhile to note that the $P2_1$ space group is polar and chiral, which is a prerequisite for magnetoelectric coupling due to the combination of ferroelectric behaviour with magnetostrictive effects [43]. Three (*S*)-L ligands and three $Dy(hfac)_3$ fragments compose the asymmetric unit (Figure 1).

Each Dy^{III} centre is octa-coordinated by six oxygen atoms from three $hfac^-$ ligands and two oxygen atoms from two phosphate groups of two different (*S*)-L ligands. The repetition of the asymmetric unit gives rise to a mono-dimensional coordination polymer. SHAPE [51] analysis suggests that all the first metal coordination spheres significantly deviate from the closest D_{4d} coordination polyhedra, although with different degrees of distortion (Table S2). Indeed, the Dy1 and Dy3 centres, respectively, show distortion degree values of 0.469 and 0.657, while Dy2 adopts a D_{4d} surrounding with a distortion degree of 0.814 close to the deviation from the C_{2v} symmetry (0.997) (Table S2). The average bond and angle values are similar for each $Dy(hfac)_3((S)\text{-}L)$ fragment. Around each Dy^{III} centre, the $Dy\text{-}O_{P=O}$ lengths (2.31(2) Å) are found to be slightly shorter than the $Dy\text{-}O_{hfac}$ distances (2.34(7) Å). The average $Dy\text{-}O_{P=O}$ length (range from 2.34(9) to 2.38(7) Å) and $_{P=O}O\text{-}Dy\text{-}O_{P=O}$ angle values (range from 141.9(8) to 146.3(7)°) are similar between the $[Dy(hfac)_3((S)\text{-}L)]$ fragments. The dihedral angle between the naphthyl groups have an average value of 85.6(4)°. The shortest intra- and inter-chain Dy-Dy distances have values of 12.144(2) Å and 11.296(2) Å, respectively. The crystal packing is driven by the formation of π-CH, F· · · F (2.718 Å) and F· · · H (2.493 Å) interactions between the polymeric chains (Figure S1). Since it was not possible to obtain **2** crystals of satisfactory quality for XRD structural determination [49], the straight relationship between structure and magnetic properties drives us to deeply compare two polymorphic structures with Dy^{III} and Eu^{III} centres. Therefore, the data at 150 K for the isostructural $[Eu(hfac)_3((S)\text{-}L)]_n$ were used. In the latter, the coordination environment is similar, with an identical bridging mode of the (*S*)-ligand. SHAPE analysis supported a more regular D_{4d} symmetry of the coordination sphere (SAPR-8 = 0.300) than what has been observed in **1**. The $_{P=O}$O-Dy-$O_{P=O}$ angle values (145.3(3)°) and dihedral angle between the naphthyl groups (77.3°) are similar in both polymorphs. The crystal packing of the **2** polymorph is also driven by very similar π-CH, F· · · F (2.718 Å) and F· · · H (2.545 Å) interactions, leading to the shortest intra- and inter-molecular Dy· · · Dy distances, respectively, equal to 12.647(2) and 11.466(2) Å, which are values close to those observed in the **1** polymorph. In summary, on one side, the SHAPE analysis demonstrated a distortion degree of the dysprosium coordination spheres stronger in **1** than for **2**, while on the other side, both crystal packings are comparable. Therefore, neither the symmetry of the coordination spheres nor the crystal packing can reasonably explain the difference of magnetic behaviour. A deeper analysis of the coordination sphere of the Dy^{III} ion in both polymorphs shows (i) close values for the angles between the plans formed by the $hfac^-$ ligand (blue one depicted in Figure S2) and the $_{P=O}$O-Dy-$O_{P=O}$ fragment (drawn in orange in the Figure S2) for both polymorphs **2** (20.6(3)°) and **1** (18.6(7)°) and (ii) significant difference of angle values calculated between the two plans formed by the two "face-to-face" $hfac^-$ ligands (drawn in green on Figure S2) for both polymorphs **2** (12.3(5)°) and **1** (26.2(9)°). In other words, the closest ideal symmetry for coordination sphere in both polymorphs is the same regardless of whether the arrangements of the ligands around the Dy^{III} centre are different, leading to different electronic distribution, and then modification in the magnetic properties could be expected.

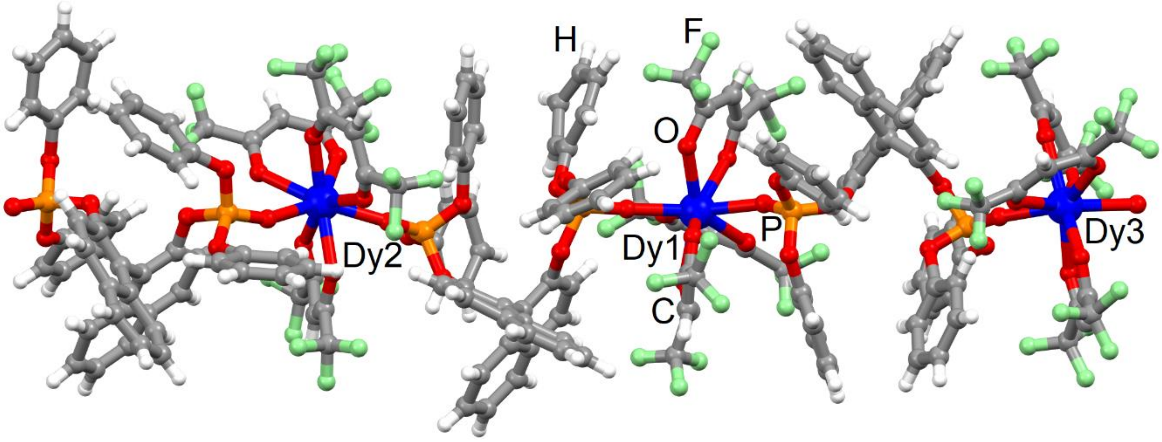

Figure 1. Asymmetric unit for the complex $[(Dy(hfac)_3((S)\text{-}L))_3]_n$ (**1**). Dy = blue, O = red, C = grey, P = orange, F = green and H = white.

Finally, the phase purity for the **1** polymorph was checked by powder X-ray diffraction (PXRD) at room temperature. This study confirmed that the single crystal structure of **1** corresponds to the bulk material and its phase purity. Both PXRD patterns of **2** and **1** were compared together with their calculated ones (from single crystal data), showing that no trace of **2** polymorph was detected in the sample of **1** (Figure S3).

2.3. Magnetic Properties

2.3.1. Static Magnetic Measurements

In Figure S4, the experimental temperature dependence of $\chi_M T$ is reported for both **2** and **1** polymorphs for comparison. It should be noted that the magnetic data are reported for 3 Dy^{III} centres for **1** to be in agreement with the proposed formula $[(Dy(hfac)_3((S)\text{-}L))_3]_n$.

For **1**, the room temperature value of 43.22 cm^3 K mol^{-1} is close to the expected one of 42.51 cm^3 K mol^{-1} for three isolated Dy^{III} ions in ^{6}H$_{15/2}$ ground multiplets [52]. On cooling down the system, the χ_MT curve decreases monotonically down to 36.93 cm^3 K mol^{-1} at 2 K. No increase in the χ_MT product is observed at low temperatures, conversely to the **2** case. This highlights the presence of different dipolar interactions in the two compounds even if the shortest intra- and inter-molecular Dy$\cdots$Dy distances were found to be similar in both polymorphs. Indeed, relative orientation of the main component of the magnetic anisotropy has a crucial role in the intensity and nature of the dipolar magnetic interaction. The field-dependence of magnetisation were measured at 2 K between 0 and 5 T for both polymorphs (Figure S5). At high fields, the magnetisation value of **1** is 15.93 Nβ, about three times the value for **2**, and far from the expected saturated value for three Dy^{III} ions of 30 Nβ, a sign of significant magnetic anisotropy.

2.3.2. Dynamic Magnetic Measurements

The **1** polymorph exhibits slow relaxation of the magnetisation in zero applied field (Figures 2a and S6). The complex **1** relaxes about 100 times slower than **2**, which was previously published at 2 K. The normalised Argand plot for **1** indicates that the observed slow magnetisation relaxation represents approximately all the signal detected in the static measurements (Figure S7). The dynamic data can be fitted with an extended Debye model (Figure S8 and Table S3). The observed thermal dependence of the extracted relaxation times (τ) could be fitted (Equation (1)) with a combination of QTM and Orbach processes using τ_{TI} = 1.57(4) × 10^{-3} s, $\tau_{0\,=}$ 1.7(2) × 10^{-5} s and Δ = 23.6(6) K (Figure S9).

$$\tau^{-1} = \underbrace{\tau_0^{-1}\exp\left(\frac{\Delta}{T}\right)}_{Orbach} + \underbrace{CT^n}_{Raman} + \underbrace{\frac{B_1}{1+B_2H^2}}_{\tau_{TI}^{-1},QTM} + \underbrace{ATH^m}_{Direct} \tag{1}$$

However, the thermal energy of the system for temperatures $\leq$12 K does not appear sufficient for activating this Orbach relaxation pathway. A more reasonable fitting procedure could consider a combination of QTM and Raman processes (Figures 3 and S10). The best fit parameters are τ_{TI} = 1.57(4) × 10^{-3} s, C = 4.0(3) s^{-1} K^{-n} and n = 3.16(3). In the case of a pure acoustic phonons (lattice vibrations) Raman process, the expected n value is 9 for Kramers ions [53], but the involvement of optical phonons (molecular vibrations) [8,15] can induce the diminution of n between 2 and 7 [54–56].

Under a static magnetic field (Figures 2b and S11), the out-of-phase maxima start to move to lower frequencies. While **2** displays a complicated relaxation dynamic, for the polymorph **1,** the field dependence of the magnetic susceptibility displays a classic behaviour. Two contributions can be distinguished for the low magnetic field values usually attributed to the presence of dipolar magnetic interactions between the Dy^{III} magnetic centres [57]. By applying field values higher than 500 Oe, only one contribution is significant. Thus, despite the presence of three independent Dy^{III} centres, only one contribution to the magnetisation relaxation is detected once the dipolar magnetic interactions are destroyed. The relaxation times are extracted from the χ_M curves using two contributions for low magnetic field values (0–400 Oe) and a single contribution for the highest magnetic field values (600–1800 Oe) (Figure S12 and Table S4). The fit output is superimposed on the argand plot in Figure S13. The field dependence of the extracted τ can be fit by Equation (2) (Figure 2c) [58,59].

$$\tau^{-1} = \frac{B_1}{1+B_2H^2} + AH^4 + k(T) \tag{2}$$

The fit parameters are B_1 = 5(1) × 10^2 s^{-1}, B_2 = 2.1(6) × 10^{-3} Oe^{-2}, A = 3.2(7) × 10^{-14} s^{-1} K^{-1} Oe^{-4} and $k(T)$ = 3(1) × 10^{-1} s^{-1}. The value of 1000 Oe was selected to study the in-field temperature-dependent behaviour of **1** (Figure 2d and Figure S14) because it is close to the optimal field and analogous to the field used in the studies for polymorph **2** [**49**]. Under

1000 Oe at 2 K, the complex **1** relaxes about 100 times slower than the slowest contribution of the polymorph **2**. Such difference has already been observed under zero applied field. Thus, the two polymorphs appear to respond in a similar way to the applied field (Figure 3). The normalised Argand plot for **1** indicates that the observed slow magnetization relaxation under an applied magnetic field represents approximately all the signal detected in the static measurements (Figure S15). The data for **1** can be interpreted with an extended Debye model (Figure S16, Table S5), accounting for only one contribution to the magnetisation relaxation in the temperature range of 2–11 K (Figure 3).

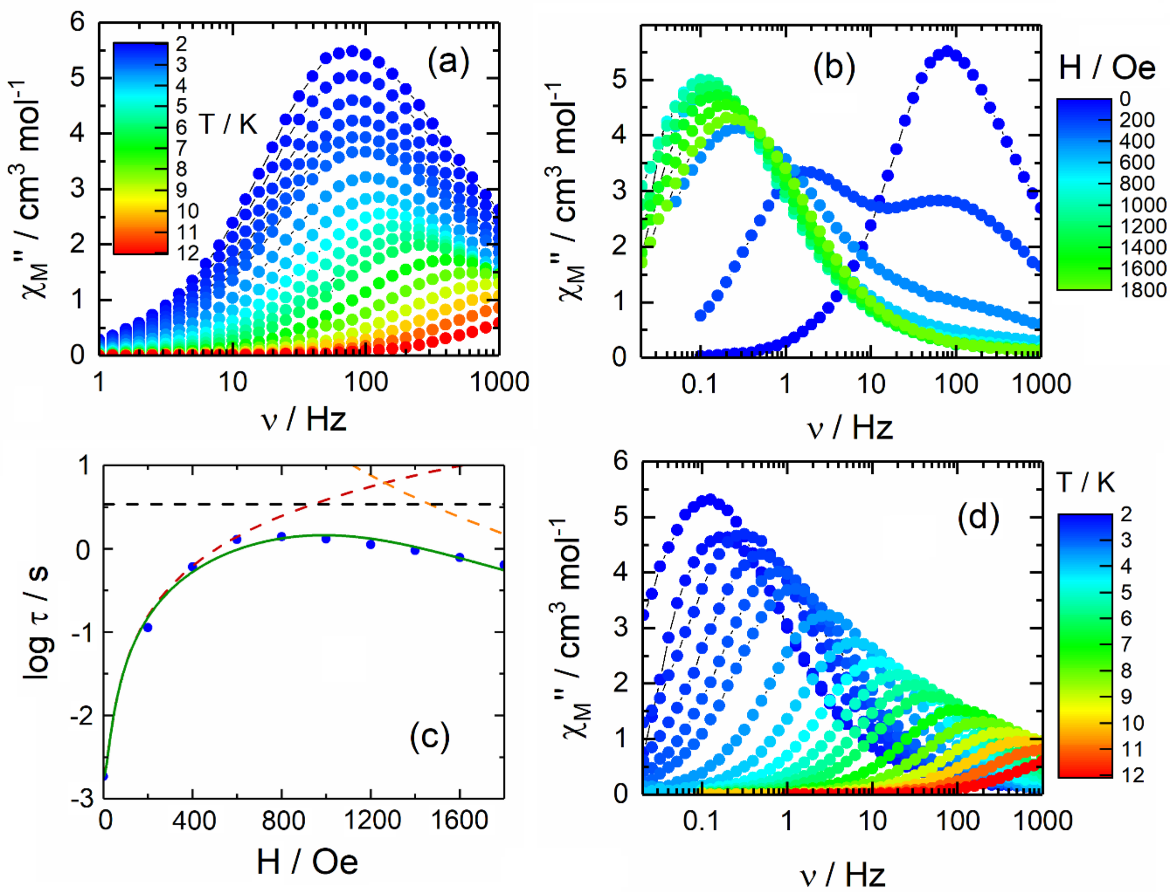

Figure 2. (**a**) Frequency dependence of χ_M'' at zero applied magnetic field for **1** in the temperature range of 2–12 K. (**b**) Frequency dependence of χ_M'' for **1** at 2 K in the 0–1800 Oe field range. (**c**) Field dependence of the relaxation time at 2 K for **1** with representation of the best fit curve (full green line) and the QTM (red dashed line), direct (orange dashed line) and thermally activated (black dashed line) contributions. (**d**) Frequency dependence of χ_M'' at 1000 Oe applied magnetic field for **1** in the temperature range 2–12 K.

The fit output is superimposed on the normalised argand plot (Figure S15). Based on the fit of the log(τ) vs. H curve (Figure 2c), no remaining QTM nor Direct processes are expected to play a major role in the magnetic relaxation. Thus, only k(T) (thermally activated Raman and Orbach processes) (Equation (2)) should be involved in the magnetic relaxation mechanism. Moreover, as previously mentioned for ac study under zero applied magnetic field, the thermal energy of the system cannot activate a similar Orbach mechanism in the studied temperatures range. Conversely, a Raman process can be satisfactorily employed to interpret the experimental log(τ) vs. T plot (Figure 3). The best fit parameters are $C = 2.6(3)\ \mathrm{s}^{-1}\ \mathrm{K}^{-n}$ and $n = 5.22(8)$. Therefore, the tunnelling phenomena observed at zero field are efficiently suppressed by applying a static dc magnetic field of 1000 Oe. The values for the Raman process is similar in both zero and applied field for temperature ranging from 612 K. Conversely to **2,** no direct pathways seem to significantly participate in the magnetisation relaxation dynamic.

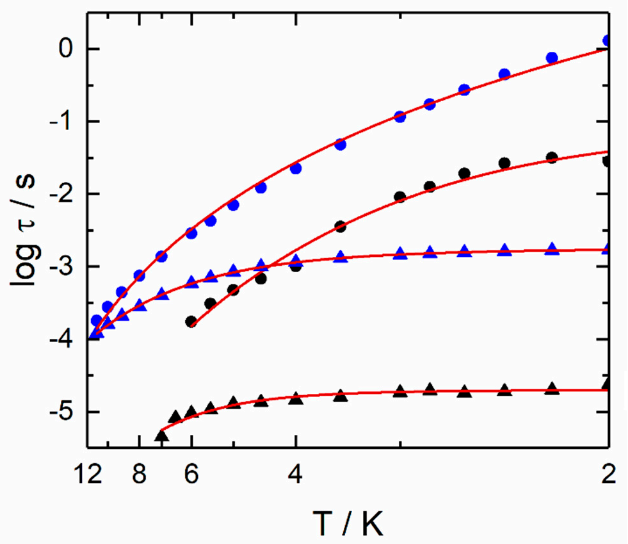

Figure 3. Temperature variation of the relaxation time for **1** (blue spots, temperature range 2–12 K) and **2** (black spots, temperature range 2–7 K) in zero (triangles) and 1000 Oe (full circles) applied magnetic field.

3. Conclusions

In this article, a new polymorph was isolated from the reaction between Dy(hfac)$_3$(H$_2$O)$_2$ and [8′-(Diphenoxylphosphinyl)[1,1′-binaphthalen]-8-yl]diphenoxylphosphine oxide ligand (**L**). The single crystal X-ray structure of [(Dy(hfac)$_3$(**L**))$_3$]$_n$ (**1**) revealed that three crystallographically independent Dy^{III} centres composed the asymmetric unit. **1** displayed slow magnetic relaxation in both zero and applied dc magnetic field. Despite the high level of distortion for the D$_{4d}$ coordination sphere around the Dy^{III} ions, the polymorph **1** displayed a slower relaxation of its magnetisation compared to the polymorph **2** which involves a more regular D$_{4d}$ surrounding. This observation was attributed to different arrangement of the coordinated ligands and a more favorable electronic distribution for **1** than **2,** demonstrating once more that the electronic distribution is more decisive than the coordination symmetry. Surprisingly, the polymorph **1** displayed one contribution for the slow magnetisation relaxation, whereas **2** displayed multi-contributions under the same applied magnetic field and this despite the presence of three different crystallographic Dy^{III} centres for **1**. The observed magnetic behaviour appears counterintuitive, and currently it cannot be fully justified. However, different magnetic dynamic properties as a consequence of differences in the dipolar interactions for similar systems were already documented [46]. This work underlines the effect of subtle structural variations on SMM behaviour.

Interestingly, the polymorph **1** crystallised in the polar chiral space group P2$_1$ and involves the hfac$^-$ ligands, which could display keto-enol transformation, allowing the switching of molecular polarity. In other words, all the needed prerequisites to observe ferroelectricity are reached [60–62]. Thus, **1** appears to be a promising candidate to the exhibition of magnetoelectric coupling [43].

4. Materials and Methods

4.1. Synthesis, General Procedures and Materials

The precursor [Dy(hfac)$_3$(H$_2$O)$_2$] (hfac$^-$ = 1,1,1,5,5,5-hexafluoroacetylacetonate anion) [63] and [8′-(Diphenoxylphosphinyl)[1,1′-binaphthalen]-8-yl]diphenoxylphosphine oxide (**L**) [64] were synthesised following previously reported methods. All other reagents were commercially available and used without further purification.

4.2. Synthesis of the Ligand [8′-(Diphenoxylphosphinyl)[1,1′-binaphthalen]-8-yl]diphenoxylphosphine Oxide (L)

Phenol in a quantity of 1.12 g (11.9 mmol) and 4.7 mL (33.7 mmol) of Et_3N were added to a solution containing 0.52 mL (5.96 mmol) of PCl_3 in 100 mL of anhydrous toluene at 0 °C under argon atmosphere. After stirring the mixture for 30 min, 0.85 g (2.97 mmol) of (S)-BINOL were added at −10 °C. The mixture was stirred for 1 h at room temperature, then filtered over Celite. The solvent was removed at reduced pressure. The residue was dissolved in EtOAc, washed with H2O, an aqueous 5% NaOCl solution and brine. The organic phase was dried with $MgSO_4$, then the solvent was removed at reduced pressure. The residue was purified by column chromatography on silica gel using petroleum ether/EtOAc (7:3) as the eluent. 0.84 g, 38% yield for (*S*)-L. ^{1}H-NMR (300 MHz, $CDCl_3$): δ = 7.93 (d, *J* = 9.0 Hz, 2 H), 7.87 (d, *J* = 8.1 Hz, 2 H), 7.78 (d, *J* = 9.0 Hz, 2 H), 7.43–7.37 (m, 2 H), 7.25–7.06 (m, 10 H), 7.00–6.98 (m, 6 H), 6.88–6.85 (m, 4 H), 6.57–6.54 (m, 4 H). ^{13}C-NMR (75 MHz, $CDCl_3$): δ = 150.3 (d, J_{CP} = 8.2 Hz), 150.1 (d, J_{CP} = 7.5 Hz), 146.7 (d, J_{CP} = 6.7 Hz), 133.6, 131.2, 130.5, 129.7, 129.5, 128.1, 127.3, 126.2, 125.8, 125.4 (d, J_{CP} = 1.5 Hz), 125.2 (d, J_{CP} = 1.5 Hz), 121.7 (d, J_{CP} = 9.0 Hz), 120.0 (d, J_{CP} = 5.2 Hz), 119.6 (d, J_{CP} = 5.2 Hz), 119.2 (d, J_{CP} = 1.5 Hz). $[\alpha]_D^{25} = +1.2$ for (*S*)-L (c = 1.0, $CHCl_3$).

4.3. Synthesis of Complex $[(Dy(hfac)_3(\mathbf{L}))_3]_n$ (1)

$[Dy(hfac)_3(H_2O)_2]$ in a quantity of 16.4 mg (0.02 mmol) was added to a solution containing 15 mg (0.02 mmol) of (*S*)-L in 2 mL of CH_2Cl_2. After 15 min of stirring, the solution was slowly evaporated, leading to a colourless and microcrystalline residue. 28.8 mg, 94% yield for **1**. I.R. (KBr, range 1800–400 cm^{-1}): 1654 (s), 1591 (m), 1556 (m), 1528 (m), 1490 (s), 1476 (m), 1459 (m), 1254 (s), 1222 (s), 1208 (s), 1194 (s), 1160 (s), 1145 (s), 1102 (m), 1078 (m), 1029 (m), 1015 (m), 1002 (m), 994 (m), 968 (m), 952 (w), 903 (w), 871 (w), 849 (w), 815 (w), 809 (w), 797 (m), 777 (m), 762 (w), 752 (m), 742 (w), 704 (w), 687 (m), 661 (m), 616 (w), 586 (m), 560 (w), 549 (w), 526 (w), 526(w), 513 (w), 500(w), 495 (w), 482 (w), 469 (w) cm^{-1}. Slow evaporation from a solution in CH_2Cl_2/*n*-hexane (1:3) led to single crystals suitable for structural X-ray studies. Anal. Calcd (%) for $C_{177}H_{104}Dy_3F_{54}O_{42}P_6$: C 46.15, H 2.26; found: C 46.32, H 2.35.

4.4. Crystallography

A single crystal of **1** was mounted on a D8 VENTURE Bruker-AXS diffractometer for data collection (MoK$_\alpha$ radiation source, λ = 0.71073 Å) at 150 K, from the Diffractometric Centre X (CDIFX), University of Rennes 1, France (Table S1). The SHELXT program [65] was used to solve the structures with a direct method and refinements were done with the SHELXL-14/7 program [66] using a full matrix least-squares method on F^2. The CCDC number is 2112160 for compound **1**. X-ray diffraction (XRD) patterns were recorded at room temperature in the 2θ range of 5–30° with a step size of 0.026° and a scan time per step of 600 s using a PANalytical X'Pert Pro diffractometer (Cu-L2,L3 radiation, λ = 1.5418 Å, 40 kV, 40 mA, PIXcel 1D detector). Data collector and HighScore Plus softwares were used, respectively, for recording and analysis of the patterns.

4.5. Physical Measurements

The elemental analyses of the compounds were performed at the Centre Régional de Mesures Physiques de l'Ouest, Rennes. The static susceptibility measurements were performed on solid polycrystalline samples with a Quantum Design MPMS-XL SQUID magnetometer. The following values of magnetic field were used: 0.2 kOe, 2 kOe and 10 kOe, respectively, for the temperature range of 2–20 K, 20–80 K and 80–300 K in order to prevent any saturation effect. The ac magnetic susceptibility measurements were both performed on a Quantum Design MPMS-XL SQUID magnetometer (1–1000 Hz frequency range). Immobilised selected and crunched single crystals were employed to realize the magnetic measurements, and the latter were all corrected for the diamagnetic contribution as calculated with Pascal's constants.

Supplementary Materials: The following are available online at https://www.mdpi.com/article/10.3390/magnetochemistry7110150/s1, Figure S1: Fragments of two chains for the complex (*S*)-**1** (view along the axis *a*). (Dy = blue, O = red, C = dark grey, H = light grey, P = orange, F = green). Figure S2: Coordination sphere of a Dy^{III} ion of **1**. P=O, the two face-to-face $hfac^-$ and the third $hfac^-$ ligands are drawn in orange, green and blue, respectively. Figure S3: Superposition of experimental powder X-ray diffraction patterns from (*S*)-**2** and (*S*)-**1** measured at 300 K and simulated from (*S*)-**2** [1] and (*S*)-**1** single-crystal data obtained at 150 K. Figure S4: Temperature dependence of the $\chi_M T$ products for (*S*)-**2** [1] and (*S*)-**1** (given for the three crystallographically independent Dy^{III} centres) in the temperature range of 2–300 K. Figure S5: Field variation of the magnetisation for (*S*)-**2** [1] and (*S*)-**1** (given for the three crystallographically independent Dy^{III} centres) in the field range of 0–5 T. Figure S6: Frequency dependence of χ'_M zero field for (*S*)-**1** in the temperature range of 1–12 K. Figure S7: Normalised argand plot of experimental (dots) and fit Debye (black lines) data for (*S*)-**1** at zero applied field in the temperature range 2–11 K. Figure S8: Frequency dependence of the in-phase (χ_M') and out-of-phase (χ_M'') components of the ac susceptibility measured on powder at 2.8 K and 0 Oe with the best fitted curves (red lines) for (*S*)-**1**. Figure S9: Temperature dependence of τ (blue spots) for (*S*)-**1** at zero applied magnetic field in the temperature range 2–11 K. The best fit curve is depicted as a full green line, and the Orbach and QTM contributions are represented, respectively, in a black dashed line and a red dashed line. Figure S10: Temperature dependence of τ (blue spots) for (*S*)-**1** at zero applied magnetic field in the temperature range 2–11 K. The best fit curve is depicted as a full green line and the Raman and QTM contributions are represented, respectively, in a black dashed line and a red dashed line. Figure S11: Frequency dependence of χ_M' for **1** at 2 K in the field range of 0–1800 Oe. Figure S12: Frequency dependence of the in-phase (χ_M') and out-of-phase (χ_M'') components of the ac susceptibility measured on powder at 2 K and 1000 Oe with the best fitted curves (red lines) for (*S*)-**1**. Figure S13: Argand plot of experimental (colored plots) and fit data (black lines) for **1** at 2 K in the field range 0–3000 Oe. Figure S14: Frequency dependence of χ_M' under an applied magnetic field of 1000 Oe for (*S*)-**1** in the temperature range of 1–12 K. Figure S15: Normalised argand plot of experimental (coloured plots) and fit data (black lines) for Dy3 under an applied magnetic field of 1000 Oe in the temperature range 2–11 K. Figure S16. Frequency dependence of the in-phase (χ_M') and out-of-phase (χ_M'') components of the ac susceptibility measured on powder at 2.8 K and 1000 Oe with the best fitted curves (red lines) for (*S*)-**1**. Table S1: X-ray crystallographic data for **1**. Table S2: SHAPE analysis of the coordination polyhedra around the $lanthanide^{III}$ centres in **1**. Table S3: Best fitted parameters (χ_T, χ_S, α and τ) with the extended Debye model for compound **1** at 0 Oe in the temperature range 2–11 K. Table S4: Best fitted parameters ($\chi_{T,1}$, χ_S, τ_1, α_1 $\chi_{T,2}$, τ_2, $\chi_{T,2}$ and α_2) with the extended Debye model for compound **1** at 2 K in the field range 0–1800 Oe. Table S5. Best fitted parameters (χ_T, χ_S, α and τ) with the extended Debye model for compound **1** at 1 kOe in the temperature range 2–11 K.

Author Contributions: C.A.M., B.L. and G.A. performed the organic syntheses and performed the coordination chemistry and crystallisations; V.D. realised the single crystal X-ray diffraction experiments and refined the X-ray structures; C.A.M. and O.C. performed and analyzed the magnetic measurements. C.L. discussed the idea and the results and commented on the manuscript. F.P. conceived and designed the experiments and contributed to the writing of the article. All authors have read and agreed to the published version of the manuscript.

Funding: This work was supported by CNRS, Université de Rennes 1, and the European Commission through the ERC-CoG 725184 MULTIPROSMM (project No. 725184).

Institutional Review Board Statement: Not applicable.

Informed Consent Statement: Not applicable.

Data Availability Statement: No data are available for this article.

Conflicts of Interest: The authors declare no conflict of interest. The founding sponsors had no role in the design of the study, the collection, analyses or interpretation of data, the writing of the manuscript or the decision to publish the results.

Abbreviations

The following abbreviations are used in this manuscript:

PXRD	Powder X-Ray Diffraction
SQUID	Superconducting Quantum Interference Device
SMM	Single Molecule Magnet
QTM	Quantum Tunneling of the Magnetisation
CH_2Cl_2	Dichloromethane
hfac^{-}	1,1,1,5,5,5-hexafluoroacetylacetonate

References

1. Sessoli, R.; Tsai, H.L.; Schake, A.R.; Wang, S.Y.; Vincent, J.B.; Folting, K.; Gatteschi, D.; Christou, G.; Hendrickson, D.N. High-spin molecules: [Mn12O12(O2CR)16(H2O)4]. *J. Am. Chem. Soc.* **1993**, *115*, 1804–1816. [CrossRef]
2. Sessoli, R.; Gatteschi, D.; Caneschi, A.; Novak, M.A. Magnetic bistability in a metal-ion cluster. *Nature* **1993**, *365*, 141–143. [CrossRef]
3. Pedersen, K.S.; Ariciu, A.-M.; McAdams, S.; Weihe, H.; Bendix, J.; Tuna, F.; Piligkos, S. Toward Molecular 4f Single-Ion Magnet Qubits. *J. Am. Chem. Soc.* **2016**, *138*, 5801–5804. [CrossRef] [PubMed]
4. Bogani, F.; Wernsdorfer, W. Molecular spintronics using single-molecule magnets. *Nat. Mater.* **2008**, *7*, 179–186. [CrossRef]
5. Vincent, R.; Klyatskaya, S.; Ruben, M.; Wernsdorfer, W.; Balestro, F. Electronic read-out of a single nuclear spin using a molecular spin transistor. *Nature* **2012**, *488*, 357–360. [CrossRef]
6. Ganzhorn, M.; Klyatskaya, S.; Ruben, M.; Wernsdorfer, W. Strong spin–phonon coupling between a single-molecule magnet and a carbon nanotube nanoelectromechanical system. *Nat. Nanotechnol.* **2013**, *8*, 165–169. [CrossRef]
7. Cornia, A.; Seneor, P. The molecular way. *Nat. Mater.* **2017**, *16*, 505–506. [CrossRef]
8. Thiele, S.; Balestro, F.; Ballou, R.; Klyatskaya, S.; Ruben, M.; Wernsdorfer, W. Electrically driven nuclear spin resonance in single-molecule magnets. *Science* **2014**, *344*, 1135–1138. [CrossRef]
9. Leuenberger, M.N.; Loss, D. Quantum computing in molecular magnets. *Nature* **2001**, *410*, 789–793. [CrossRef]
10. Ardavan, A.; Rival, O.; Morton, J.J.L.; Blundell, S.J.; Tyryshkin, A.M.; Timco, G.A.; Winpenny, R.E.P. Will Spin-Relaxation Times in Molecular Magnets Permit Quantum Information Processing? *Phys. Rev. Lett.* **2007**, *98*, 057201. [CrossRef] [PubMed]
11. Stamp, P.C.E.; Gaita-Ariño, A. Spin-based quantum computers made by chemistry: Hows and whys. *J. Mater. Chem.* **2009**, *19*, 1718–1730. [CrossRef]
12. Martínez-Pérez, M.J.; Cardona-Serra, S.; Schlegel, C.; Moro, F.; Alonso, P.J.; Prima-García, H.; Clemente-Juan, J.M.; Evangelisti, M.; Gaita-Arino, A.; Sesé, J.; et al. Gd-Based Single-Ion Magnets with Tunable Magnetic Anisotropy: Molecular Design of Spin Qubits. *Phys. Rev. Lett.* **2012**, *108*, 247213. [CrossRef] [PubMed]
13. Sessoli, R.; Boulon, M.-E.; Caneschi, A.; Mannini, M.; Poggini, L.; Wilhelm, F.; Rogalev, A. Strong magnetochiral dichroism in a paramagnetic molecular helix observed by hard X-rays. *Nat. Phys.* **2015**, *11*, 69–74. [CrossRef] [PubMed]
14. Ishikawa, N.; Sugita, M.; Ishikawa, T.; Koshihara, S.; Kaizu, Y. Lanthanide Double-Decker Complexes Functioning as Magnets at the Single-Molecular Level. *J. Am. Chem. Soc.* **2003**, *125*, 8694–8695. [CrossRef] [PubMed]
15. Guo, F.-S.; Day, B.-M.; Chen, Y.-C.; Tong, M.-L.; Mansikkamäki, A.; Layfield, R.A. Magnetic hysteresis up to 80 kelvin in a dysprosium metallocene single-molecule magnet. *Science* **2018**, *362*, 1400–1403. [CrossRef]
16. Mannini, M.; Pineider, F.; Sainctavit, P.; Danieli, C.; Otero, E.; Sciancalepore, C.; Talarico, A.M.; Arrio, M.-A.; Cornia, A.; Gatteschi, D.; et al. Magnetic memory of a single-molecule quantum magnet wired to a gold surface. *Nat. Mater.* **2009**, *8*, 194–197. [CrossRef]
17. Affronte, M. Molecular nanomagnets for information technologies. *J. Mater. Chem.* **2009**, *19*, 1731–1737. [CrossRef]
18. Coronado, E.; Forment-Aliaga, A.; Galán-Mascarós, J.R.; Giménez-Saiz, C.; Gómez-Garcia, C.J.; Martinéz-Ferrero, E.; Nuez, A.; Romero, F.M. Multifunctional molecular materials. *Solid State Sci.* **2003**, *5*, 917–924. [CrossRef]
19. Coronado, E.; Giménez-Saiz, C.; Martí-Gastaldo, C. Crystal engineering of multifunctional molecular materials. In *Engineering of Crystalline Materials Properties*; Novoa, J.J., Braga, D., Addadi, L., Eds.; NATO Science for Peace and Security Series B: Physics and Biophysics; Springer: Dordrecht, The Netherlands, 2008; pp. 173–191.
20. Coronado, E.; Palacio, F.; Veciana, J. Molecule–Based Magnetic Materials. *Angew. Chem. Int. Ed.* **2003**, *42*, 2570–2572. [CrossRef]
21. Gómez-Romero, P.; Sánchez, C. *Functional Hybrids Materials*; Wiley-VCH: Weinheim, Germany, 2004.
22. Fahmi, A.; Pietsch, T.; Mendoza, C.; Cheval, N. Functional hybrid materials. *Mater. Today* **2009**, *12*, 44–50. [CrossRef]
23. Rocha, J.; Carlos, L.D.; Paz, F.A.A.; Ananias, D. Luminescent progress in hybrid materials science. *Chem. Soc. Rev.* **2011**, *40*, 926–940. [CrossRef]
24. Sanchez, C.; Shea, K.J.; Kitagawa, S. Recent progress in hybrid materials science. *Chem. Soc. Rev.* **2011**, *40*, 471–472. [CrossRef]
25. Ouahab, L. *Multifunctional Molecular Materials*; Taylor and Francis Group CRC Press: New York, NY, USA, 2012.
26. Scott, J.F. Applications of Modern Ferroelectrics. *Science* **2007**, *315*, 954–959. [CrossRef]
27. Tsymbal, E.Y.; Kohlstedt, H. Tunneling Across a Ferroelectric. *Science* **2006**, *313*, 181–183. [CrossRef]
28. Cheong, S.-W.; Mostovoy, M. Multiferroics: A magnetic twist for ferroelectricity. *Nat. Mater.* **2007**, *6*, 13–20. [CrossRef] [PubMed]
29. Ramesh, R.; Spaldin, N.A. Multiferroics: Progress and prospects in thin films. *Nat. Mater.* **2007**, *6*, 21–29. [CrossRef] [PubMed]
30. Rikken, G.L.J.A.; Raupach, E. Observation of magneto-chiral dichroism. *Nature* **1997**, *390*, 493–494. [CrossRef]
31. Barron, L.D. Chirality, magnetism and light. *Nature* **2000**, *405*, 895–896. [CrossRef]
32. Train, C.; Gheorghe, R.; Krstic, V.; Chamoreau, L.; Ovnesyan, N.S.; Rikken, G.L.J.A.; Gruselle, M.; Verdaguer, M. Strong magneto-chiral dichroism in enantiopure chiral ferromagnets. *Nat. Mater.* **2008**, *7*, 729–734. [CrossRef]

33. Bordács, S.; Kézsmárki, I.; Szaller, D.; Demkó, L.; Kida, N.; Murakawa, H.; Onose, Y. Chirality of matter shows up via spin excitations. *Nat. Phys.* **2012**, *8*, 734–738. [CrossRef]
34. El Rez, B.; Liu, J.; Béreau, V.; Duhayon, C.; Horino, Y.; Suzuki, T.; Coolen, L.; Sutter, J.-P. Concomitant emergence of circularly polarized luminescence and single-molecule magnet behavior in chiral-at-metal Dy complex. *Inorg. Chem. Front.* **2020**, *7*, 4527–4534. [CrossRef]
35. Huizi-Rayo, U.; Zabala-Lekuona, A.; Terenzi, A.; Cruz, C.M.; Cuerva, J.M.; Rodriguez-Diéguez, A.; Garcia, J.A.; Seco, J.M.; San Sebastian, E.; Cepeda, J. Influence of thermally induced structural transformations on the magnetic and luminescence properties of tartrate-based chiral lanthanide organic-frameworks. *J. Mater. Chem. C.* **2020**, *8*, 8243–8256. [CrossRef]
36. Gendron, F.; Di Pietro, S.; Abad Galan, L.; Riobé, F.; Placide, V.; Guy, L.; Zinna, F.; Di Bari, L.; Bensalah-Ledoux, A.; Guyot, Y.; et al. Luminescence, chiroptical, magnetic and ab initio crystal-field characterizations of an enantiopure helicoidal Yb(III) complex. *Inorg. Chem. Front.* **2021**, *8*, 914–926. [CrossRef]
37. Lefeuvre, B.; Mattei, C.A.; Flores Gonzalez, J.; Gendron, F.; Dorcet, V.; Riobé, F.; Lalli, C.; Le Guennic, B.; Cador, O.; Maury, O.; et al. Solid-State near-Infrared Circularly Polarized Luminescence from Chiral $\mathrm{Yb^{III}}$-Single-Molecule Magnet. *Chem. Eur. J.* **2021**, *27*, 7362–7366. [CrossRef] [PubMed]
38. Li, D.-P.; Wang, T.-W.; Li, C.-H.; Liu, D.-S.; Li, Y.-Z.; You, X.-Z. Single-ion magnets based on mononuclear lanthanide complexes with chiral Schiff base ligands [Ln(FTA)3L] (Ln = Sm, Eu, Gd, Tb and Dy). *Chem. Commun.* **2010**, *46*, 2929–2931. [CrossRef] [PubMed]
39. Li, X.-L.; Chen, C.-L.; Gao, Y.-L.; Liu, C.-M.; Feng, X.-L.; Gui, Y.-H.; Fang, S.-M. Modulation of Homochiral $\mathrm{Dy^{III}}$ Complexes: Single–Molecule Magnets with Ferroelectric Properties. *Chem.–A Eur. J.* **2012**, *18*, 14632–14637. [CrossRef] [PubMed]
40. Li, X.-L.; Chen, C.-L.; Xiao, H.-P.; Wang, A.-L.; Liu, C.-M.; Zheng, X.; Gao, L.-J.; Yang, X.-G.; Fang, S.-M. Luminescent, magnetic and ferroelectric properties of noncentrosymmetric chain-like complexes composed of nine-coordinate lanthanide ions. *Dalton Trans.* **2013**, *42*, 15325–15347. [CrossRef] [PubMed]
41. Long, J.; Rouquette, J.; Thibaud, J.-M.; Ferreira, R.A.S.; Carlos, L.D.; Donnadieu, B.; Vieru, V.; Chibotaru, L.F.; Konczewicz, L.; Haines, J.; et al. A High–Temperature Molecular Ferroelectric Zn/Dy Complex Exhibiting Single–Ion–Magnet Behavior and Lanthanide Luminescence. *Angew. Chem. Int. Ed.* **2015**, *54*, 2236–2240. [CrossRef]
42. Li, X.-L.; Hu, M.; Yin, Z.; Zhu, C.; Liu, C.-M.; Xiao, H.-P.; Fang, S. Enhanced single-ion magnetic and ferroelectric properties of mononuclear Dy(III) enantiomeric pairs through the coordination role of chiral ligands. *Chem. Commun.* **2017**, *53*, 3998–4001. [CrossRef]
43. Long, J.; Ivanov, M.S.; Khomchenko, V.A.; Mamontova, E.; Thibaud, J.-M.; Rouquette, J.; Beaudhuin, M.; Granier, D.; Ferreira, R.A.S.; Carlos, L.D.; et al. Room temperature magnetoelectric coupling in a molecular ferroelectric ytterbium(III) complex. *Science* **2020**, *367*, 671–676. [CrossRef]
44. Wang, K.; Zeng, S.; Wang, H.; Dou, J.; Jiang, J. Magnetochiral dichroism in chiral mixed (phthalocyaninato)(porphyrinato) rare earth triple-decker SMMs. *Inorg. Chem. Front.* **2014**, *1*, 167–171. [CrossRef]
45. Atzori, M.; Dhbaibi, K.; Douib, H.; Grasser, M.; Dorcet, V.; Breslavetz, I.; Paillot, K.; Cador, O.; Rikken, G.L.J.A.; Le Guennic, B.; et al. Helicene-Based Ligands Enable Strong Magneto-Chiral Dichroism in a Chiral Ytterbium Complex. *J. Am. Chem. Soc.* **2021**, *143*, 2671–2675. [CrossRef]
46. Ou-Yang, J.-K.; Saleh, N.; Fernandez Garcia, G.; Norel, L.; Pointillart, F.; Guizouarn, T.; Cador, O.; Totti, F.; Ouahab, L.; Crassous, J.; et al. Improved slow magnetic relaxation in optically pure helicene-based $\mathrm{Dy^{III}}$ single molecule magnets. *Chem. Commun.* **2016**, *52*, 14474–14477. [CrossRef] [PubMed]
47. Pointillart, F.; Bernot, K.; Poneti, G.; Sessoli, R. Crystal Packing Effects on the Magnetic Slow Relaxation of Tb(III)-Nitronyl Nitroxide Radical Cyclic Dinuclear Clusters. *Inorg. Chem.* **2012**, *51*, 12218–12229. [CrossRef]
48. Kishi, Y.; Pointillart, F.; Lefeuvre, B.; Riobé, F.; Le Guennic, B.; Golhen, S.; Cador, O.; Maury, O.; Fujiwara, H.; Ouahab, L. Isotopically enriched polymorphs of dysprosium single molecule magnets. *Chem. Commun.* **2017**, *53*, 3575–3578. [CrossRef]
49. Mattei, C.A.; Montigaud, V.; Gendron, F.; Denis-Quanquin, S.; Dorcet, V.; Giraud, N.; Riobé, F.; Argouarch, G.; Maury, O.; Le Guennic, B.; et al. Solid-state versus solution investigation of a luminescent chiral BINOL-derived bisphosphate single-molecule magnet. *Inorg. Chem. Front.* **2021**, *8*, 947–962. [CrossRef]
50. Mattei, C.A.; Montigaud, V.; Dorcet, V.; Riobé, F.; Argouarch, G.; Maury, O.; Le Guennic, B.; Cador, O.; Lalli, C.; Pointillart, F. Luminescent dysprosium single-molecule magnets made from designed chiral BINOL-derived bisphosphate ligands. *Inorg. Chem. Front.* **2021**, *8*, 963–976. [CrossRef]
51. Llunell, M.; Casanova, D.; Cirera, J.; Alemany, P.; Alvarez, S. *SHAPE Program for the Stereochemical Analysis of Molecular Fragments by Means of Continuous Shape Measures and Associated Tools*; Departament de Quimica Fisica, Departament de Quimica Inorganica, and Institut de Quimica Teorica i Computacional–Universitat dè Barcelona: Barcelona, Spain, 2013.
52. Kahn, O. *Molecular Magnetism*; VCH: Weinhem, Germany, 1993.
53. Abragam, A.; Bleaney, B. *Electron Paramagnetic Resonance of Transition Ions*; Clarendon Press: Oxford, UK, 1970.
54. Singh, A.; Shrivastava, K.N. Optical-acoustic two-phonon relaxation in spin systems. *Phys. Status Solidi B* **1979**, *95*, 273–277. [CrossRef]
55. Shirivastava, K.N. Theory of Spin-Lattice Relaxation. *Phys. Status Solidi B* **1983**, *177*, 437. [CrossRef]
56. Evans, P.; Reta, D.; Whitehead, G.F.S.; Chilton, N.F.; Mills, D.P. Bis-Monophospholyl Dysprosium Cation Showing Magnetic Hysteresis at 48 K. *J. Am. Chem. Soc.* **2019**, *141*, 19935–19940. [CrossRef]

57. Pointillart, F.; Bernot, K.; Golhen, S.; Le Guennic, B.; Guizouarn, T.; Ouahab, L.; Cador, O. Magnetic memory in an Isotopically Enriched and Magnetically Isolated Mononuclear Dysprosium Complex. *Angew. Chem. Int. Ed.* **2015**, *54*, 1504–1507. [CrossRef]
58. Pointillart, F.; Flores Gonzalez, J.; Montigaud, V.; Tesi, L.; Cherkasov, V.; Le Guennic, B.; Cador, O.; Ouahab, L.; Sessoli, R.; Kuropatov, V. Redox- and solvato-magnetic switching in a tetrathiafulvalene-based triad single-molecule magnet. *Inorg. Chem. Front.* **2020**, *7*, 2322–2334. [CrossRef]
59. Car, P.-E.; Perfetti, M.; Mannini, M.; Favre, A.; Caneschi, A.; Sessoli, R. Giant field dependence of the low temperature relaxation of the magnetization in a dysprosium(iii)–DOTA complex. *Chem. Commun.* **2011**, *47*, 3751–3753. [CrossRef] [PubMed]
60. Fu, D.-W.; Song, Y.-M.; Wang, G.-X.; Ye, Q.; Xiong, R.-G.; Akutagawa, T.; Nakamura, T.; Chan, P.W.H.; Huang, S.D. Dielectric Anisotropy of a Homochiral Trinuclear Nickel(II) Complex. *J. Am. Chem. Soc.* **2007**, *129*, 5346–5347. [CrossRef]
61. Li, X.-L.; Chen, K.; Liu, Y.; Wang, Z.-X.; Wang, T.-W.; Zuo, J.-L.; Li, -Z.; Wang, Y.; Zhu, J.-S.; Liu, J.-M.; et al. Molecule-Based Ferroelectric Thin Films: Mononuclear Lanthanide Enantiomers Displaying Room-Temperature Ferroelectric and Dielectric Properties. *Angew. Chem. Int. Ed.* **2007**, *46*, 6820–6823. [CrossRef]
62. Horiuchi, S.; Tokunaga, Y.; Giovannetti, G.; Piccozzi, S.; Itoh, H.; Shimano, R.; Kumai, R.; Tokura, Y. Above-room-temperature ferroelectricity in a single-component molecular crystal. *Nature* **2010**, *463*, 789–792. [CrossRef] [PubMed]
63. Richardson, M.F.; Wagner, W.F.; Sands, D.E. Rare earth trishexafluoroacetylacetonates and related compounds. *J. Inorg. Nucl. Chem.* **1968**, *30*, 1275–1289. [CrossRef]
64. Ngo Ndimba, A.; Roisnel, T.; Argouarch, G.; Lalli, C. Harvesting New Chiral Phosphotriesters by Phosphorylation of BINOL and Parent Bis-phenols. *Synthesis* **2019**, *51*, 865–873.
65. Sheldrick, G.M. SHELXT—Integrated space-group and crystal-structure determination. *Acta Crystallogr. Sect. A Found. Adv.* **2015**, *71*, 3–8. [CrossRef]
66. Sheldrick, G.M. Crystal structure refinement with SHELXL. *Acta Crystallogr. Sect. C Struct. Chem.* **2015**, *71*, 3–8. [CrossRef]